Materials Advances

ROYAL SOCIETY OF CHEMISTRY

PAPER

View Article Online
View Journal | View Issue

Cite this: *Mater. Adv.*, 2025, 6, 5100

Sensing of ultra-ppm level NO_2 gas *via* synergistic effects of Cr doping and e-beam irradiation in WO_3 nanostructures†

Anusha, [a] P. Poornesh, *[a] Vikash Chandra Petwal,[b] Vijay Pal Verma[b] and Jishnu Dwivedi[b]

Herein, we report the effects of Cr doping and electron beam irradiation (EBI) on WO_3 thin films towards low-level detection of NO_2. Structural, morphological, and defect correlations are presented to provide a comprehensive understanding of the film's properties. XRD and Raman analyses confirmed the formation of well-crystallized WO_3 films due to doping and irradiation. Photoluminescence analysis validated the presence of oxygen vacancy (V_o) defects in the films which was further corroborated by XPS studies. The EBI Cr–WO_3 film exhibited a higher concentration of V_o defects and smaller grain sizes, contributing to enhanced sensing performance. A maximum sensor response of 3.43 was achieved at an NO_2 concentration of 5 ppm. Theoretical limit of detection (LOD) calculations indicated ultra-low NO_2 detection capability at 0.4 ppm (400 ppb), highlighting the potential of the prepared film for applications in environmental monitoring, healthcare diagnostics, and industrial settings.

Received 5th April 2025,
Accepted 17th June 2025

DOI: 10.1039/d5ma00330j

rsc.li/materials-advances

1. Introduction

Recently, ambient air pollution has emerged as a severe global issue, adversely affecting human health in multiple ways, such as causing heart disease, stroke, and lung diseases like asthma and cancer, ultimately leading to death.[1–3] According to a 2019 survey conducted by the World Health Organization (WHO), a striking 99% of the global population resided in areas where air quality did not meet WHO guidelines.[4] The primary pollutants contributing to this situation include particulate matter (PM), nitrogen dioxide (NO_2), sulfur dioxide (SO_2), and carbon monoxide (CO). Among them, NO_2 is a significant air pollutant primarily released from vehicles, industrial operations, fossil fuel combustion and nuclear power plants.[5] The Occupational Safety and Health Administration (OSHA) recommends that the permissible exposure limit for NO_2 must be maintained below 5 ppm.[6] Exceeding this limit can result in severe cardiovascular and respiratory diseases, while also contributing to environmental issues such as acid rain and photochemical smog, posing serious risks to both human health and the ecosystem. Moreover, recent research highlights a correlation between ambient NO_2 levels and increased disease severity in COVID-19 patients.[7]

To overcome these problems, the field of materials science has developed various metal oxide semiconductor (MOS)-based gas sensors using SnO_2,[8] WO_3,[9] ZnO,[10] TiO_2,[11] CuO.[12] MOS sensors are favoured for their excellent sensitivity, chemical stability, and ease of fabrication. They typically operate on the chemiresistive principle, wherein the adsorption of gas molecules onto the surface alters the electrical resistance of the sensing layer through surface reactions and modulation of charge carriers.[13,14] A more detailed explanation of the sensing mechanism is provided in Section 3.6.2. In recent years, tungsten oxide (WO_3)-based gas sensors have garnered considerable attention within the research community owing to their superior catalytic properties, structural stability, and the presence of oxygen vacancy defects.[15–17] To further enhance the sensing performance of WO_3, various modification strategies such as doping, composite formation, heterojunction engineering, and irradiation have been employed.[18–22] For example, Hingangavkar *et al.*[3] synthesized WO_3–rGO composite to detect NO_2 at a working temperature of 150 °C. The sensor exhibited a response of 2.52 towards 100 ppm NO_2. Rossinyol *et al.*[23] prepared Cr-doped WO_3 thin films and tested them towards a low concentration of NO_2 at 230 °C. Sensors marked the slow recovery of 16 min towards 0.1 ppm NO_2. Similarly, Mathankumar *et al.*[24] fabricated Y-doped WO_3 sensors for NO_2 detection. Increased oxygen vacancies were observed upon doping, leading to a substantial improvement in sensor response. On the other hand, Lee *et al.*[25] investigated the

[a] *Department of Physics, Manipal Institute of Technology, Manipal Academy of Higher Education, Manipal, Karnataka 576104, India. E-mail: poornesh.p@manipal.edu, poorneshp@gmail.com*
[b] *Industrial Accelerator Section, PSIAD, Raja Ramanna Centre for Advanced Technology, Indore 452012, M.P., India*

† Electronic supplementary information (ESI) available. See DOI: https://doi.org/10.1039/d5ma00330j

NO_2 sensing behaviour of WO_3 films decorated with carbon nanofibers and subsequently subjected to UV irradiation. They reported a detection limit of 1 ppm at room temperature, though the sensor demonstrated a prolonged recovery time of 7 minutes. Zhang *et al.*[22] utilized laser irradiation to enhance the NO_2 sensing performance of WO_3 films at 200 °C, achieving a 4.3-fold increase in sensor response. These findings suggest that doping, composite formation, and irradiation significantly alter the properties of WO_3, resulting in enhanced sensor performance. Nevertheless, considering the hazardous effects of NO_2, there remains a pressing need for WO_3-based sensors with improved sensitivity and rapid response/recovery characteristics at optimal operating temperatures.

In this study, we present a novel approach to enhance the NO_2 sensing characteristics of WO_3 films through the combined effects of chromium doping and electron beam irradiation. The films were evaluated for their response to low concentrations (1–5 ppm) of NO_2 at an optimal operating temperature of 200 °C. Furthermore, we established structure–property correlations related to the sensing features.

2. Experimental section

2.1 Materials and methods

Ammonium metatungstate hydrate (AMT) [$(NH_4)_6H_2W_{12}O_{40}\cdot xH_2O$, 99.99%] from Sigma-Aldrich, chromium(III) nitrate nonahydrate [$Cr(NO_3)_3\cdot 9H_2O$, 99%] from Sigma-Aldrich, polyethylene glycol 400 (PEG 400) [$H(OCH_2CH_2)_nOH$] from Molychem, nitric acid [HNO_3, 69%] from Merck Life Science Pvt. Ltd were used without further processing.

To synthesize WO_3 films, AMT was dissolved in doubly distilled water to achieve 0.01 M concentration. To improve the adhesion properties, PEG 400 and a few drops of conc. HNO_3 were added maintaining the solution's pH at ~3. The solution was stirred for about 30 minutes in a magnetic stirrer to get a homogeneous mixture. For Cr-doped WO_3 (Cr–WO_3), the same procedure was followed, incorporating a chromium precursor into the AMT solution. The films were then deposited onto a soda lime glass substrate by employing the spray pyrolysis technique. Spray pyrolysis is a low-cost, scalable, and versatile technique that enables uniform deposition of oxide thin films with controlled composition and doping. Its simplicity and adaptability make it highly suitable for fabricating gas sensing materials. The deposition temperature was set at 400 °C and air pressure was adjusted to 0.4 bar to get the uniform films with an approximate thickness of 600 nm.

Electron beam irradiation (EBI) was conducted using a LINAC accelerator, with an 8 MeV electron beam irradiated onto the Cr–WO_3 film. For clarity and ease of reference, the WO_3, Cr–WO_3, and electron beam irradiated Cr–WO_3 films are denoted as sample A, sample B, and sample C, respectively, throughout the manuscript. The detailed composition and treatment conditions are summarized in Table 1. Fig. 1 illustrates the film synthesis procedure employed in the present study.

Table 1 Summary of sample names with composition and treatment details

Sample name	Composition	Post-treatment
Sample A	Pure WO_3	None
Sample B	WO_3 + 3 wt% Cr	None
Sample C	WO_3 + 3 wt% Cr	Electron beam irradiation (8 MeV, 10 kGy)

2.2 Materials characterization details

X-ray diffraction (XRD) analysis [Rigaku SmartLab] was performed over a 2θ range of 20°–80° at 40 kV and 30 mA using Cu-Kα radiation (λ = 1.54 Å) to determine structural and phase information. Raman spectroscopy [Horiba Lab Ram HR] was

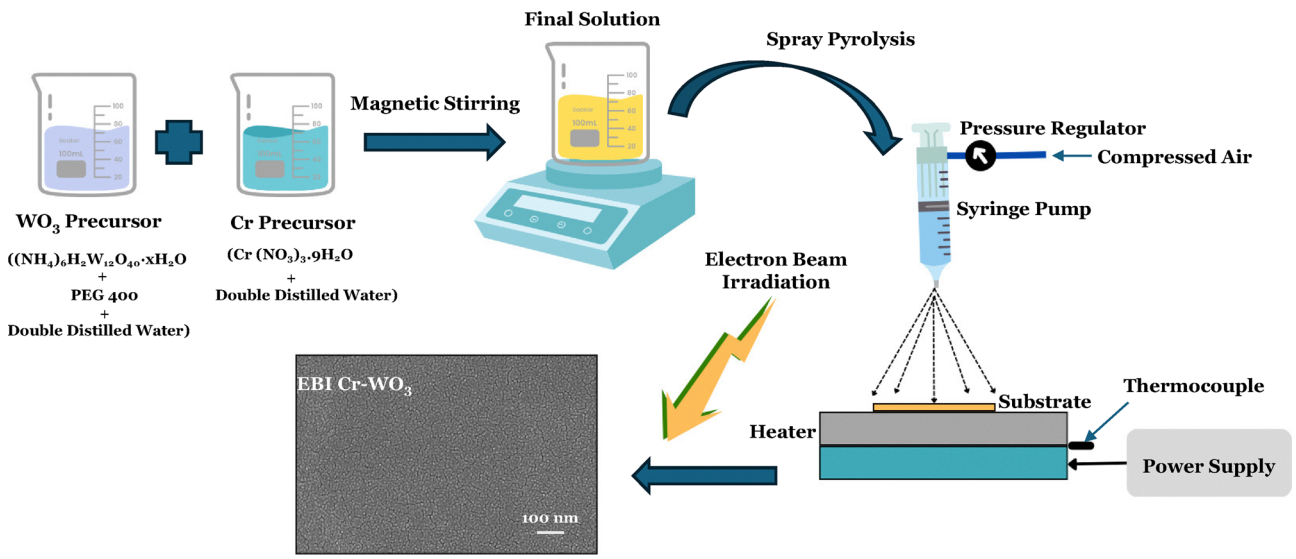

Fig. 1 Synthesis process of the sensing layer in this study.

implemented utilizing a 532 nm laser source to gain additional insights into the structure, defects, and the presence of various modes of vibrations in the samples. UV-Visible spectrophotometry [Shimadzu 1800] was employed to determine the bandgap of the samples (Section S2, ESI†). Photoluminescence (PL) measurements [JASCO FP-8500] were performed using a xenon lamp excitation source at a wavelength of 256 nm to analyze the defect states present in the samples. Morphological features were examined *via* field emission scanning electron microscopy (FESEM) [ZEISS ULTRA55]. X-ray photoelectron spectroscopy (XPS) [Kratos AXIS ULTRA] with Al-Kα source (λ = 1486.6 eV) was used to identify the oxidation state of the elements and perform composition studies on the samples.

2.3 Gas sensing measurements

Films with dimensions of 1 cm × 1 cm were used for the sensing tests. Silver paste electrodes (Alfa Aesar) were applied to the film surface, maintaining a 5 mm distance between them. The film was placed inside a chamber on a graphite block equipped with a lamp that served as a heater. A constant gas flow of 500 sccm was maintained within the chamber using programmable mass flow controllers (MFCs, Alicat Scientific). The sensor's operating temperature was optimized between room temperature and 250 °C. At lower temperatures, the response was negligible due to poor recovery behaviour. A significant and stable response, along with faster recovery, was observed at 200 °C, which was therefore selected for all subsequent measurements.

The sensor film was alternately exposed to dry air (79% N_2 + 21% O_2) and the target gas (NO_2) to record measurements. Dry air was purged until stabilization was achieved, after which NO_2 was introduced until a stable response was noted. Current–voltage (*I*–*V*) characteristics were recorded using a Keithley 2450 source meter to evaluate the sensor's response to the target gas. The diagrammatic representation of the gas sensor set-up used in the present study is shown in Fig. 2.

3. Results and discussion

3.1 Structural insights from XRD

X-ray diffraction (XRD) analysis was performed to investigate the structural modifications in the WO_3 film caused by chromium doping and electron beam irradiation. Fig. 3(a) presents the XRD patterns of samples A, B and C respectively. XRD pattern exhibits a prominent peak (200) at ~24.63° and several minor peaks suggesting the polycrystalline nature of the films. No secondary phase related to WO_3/Cr was detected, indicating that the deposited samples were free from impurities. All the diffraction peaks were matched with ICDD 43-1035, according to which the samples exhibit a monoclinic (γ) structure.[26–28]

Various structural parameters derived from XRD patterns using the eqn (S1)–(S3) (ESI†) and are summarised in Table 2. The systematic increase in crystallite size (D) values from 12 nm to 16 nm is evident, accompanied by a concurrent reduction in dislocation density (δ) and strain (ε) values. Due to the slight difference in ionic radii of the host and dopant ions (r_{Cr}^{3+} = 0.62 Å; r_W^{6+} = 0.60 Å), only minor reductions in strain and dislocation density were observed upon Cr incorporation into the WO_3 matrix.[29,30] However, the introduction of EBI into the Cr–WO_3 matrix induced further reduction in the strain and dislocation defects along with the left shift of the major peak (200) (Fig. 3(b)). The higher energy electron beam can cause point defects or vacancies, resulting in lattice expansion as substantiated by increased lattice plane distance (d) value (Table 2) and associated shift in the XRD peak.[31] The reduced lattice strain due to EBI can be attributed to a localized stress relaxation mechanism, likely driven by defect redistribution and structural reorganization.[32,33] During e-beam treatment, the transfer of momentum and energy induces the formation of vacancies and self-interstitials, which are subsequently partially removed *via* a diffusion-controlled mechanism. This defect reduction process leads to strain relaxation and improved crystallinity, as evidenced by the decrease in full-width at half-maximum (FWHM) values and the corresponding increase in crystallite size. Specifically, the FWHM values of the (200)

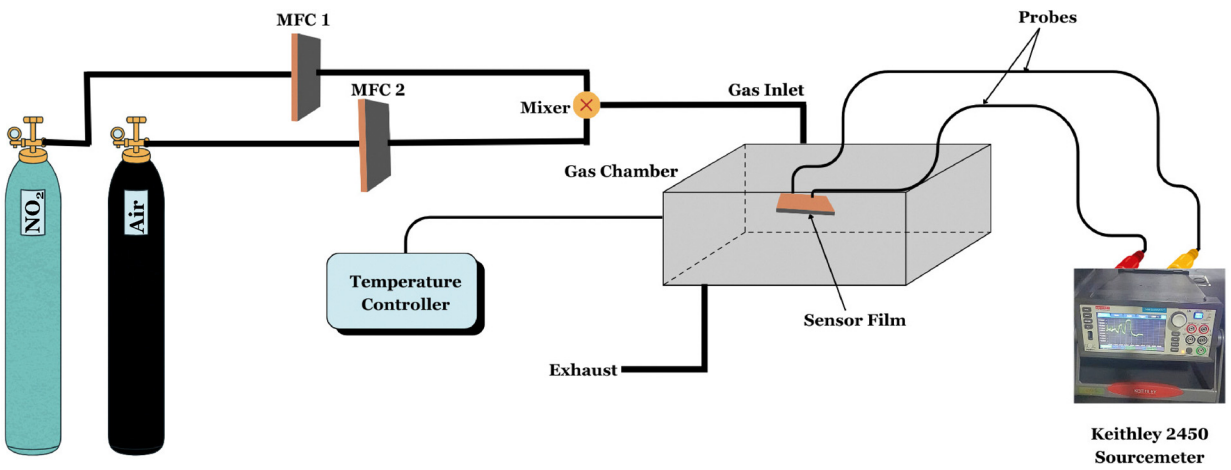

Fig. 2 Schematic diagram illustrating the configuration of the gas sensing system.

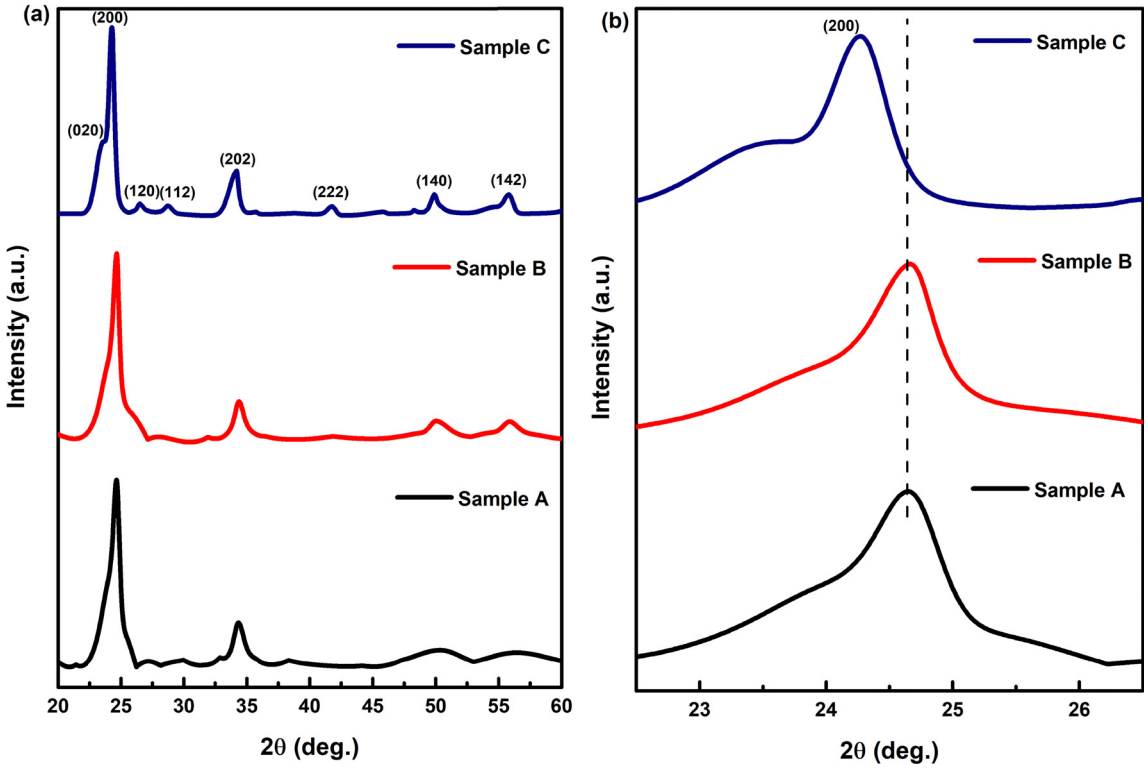

Fig. 3 (a) XRD patterns of samples A, B and C. (b) Enlarged view of peak (200).

Table 2 Structural parameters evaluated from XRD

Sample name	d spacing (Å)	Crystallite size D (nm)	Dislocation density δ ($\times 10^{15}$ lines per m^2)	Strain ε ($\times 10^{-2}$)
Sample A	3.61	12	7.16	1.37
Sample B	3.61	13	5.88	1.24
Sample C	3.66	16	3.96	1.04

peak were found to decrease progressively from 0.69 for sample A to 0.62 for sample B and 0.51 for sample C.

3.2 Structural insights from Raman

Structure confirmation and defects induced were further verified *via* Raman spectra as illustrated in Fig. 4(a). According to group theory, monoclinic WO_3 with $P2_1/n$ space group and $C_{2h}{}^5$ point group has phonon zone centers given by,[34]

$$\Gamma_{\text{phonons}} = 24(A_g + A_u + B_g + B_u) \quad (1)$$

In the above equation, 48 zone centers were assigned to Raman active modes (A_g and B_g) and remaining related to acoustic and infrared (IR) active modes. The Raman modes associated with A_g symmetry are the most commonly reported WO_3 modes in the literature.[35–37] This predominance arises from the fact that B_g modes exhibit significantly lower intensity, making them difficult to detect in Raman spectra. In the present study, characteristic monoclinic WO_3 peaks were observed at approximately 112, 134, 273, 327, 716, 805, and 961 cm^{-1}, corresponding to various vibrational modes within the WO_3 lattice. The peaks observed at approximately 716 and 805 cm^{-1} correspond to the asymmetric and symmetric stretching vibrations (ν_{as} and ν_s) of the O–W–O bonds, which represent the most prominent modes of monoclinic WO_3.[35] Peaks at 273 and 327 cm^{-1} are linked to the bending vibrations (δ) of the O–W–O bonds, while those below 200 cm^{-1} are associated with lattice vibrational modes.[38,39] Additionally, a peak at 961 cm^{-1} was consistently detected in all the films, indicating a symmetric stretching vibration of the terminal W=O bonds. Table 3 depicts the Raman peak assignments and corresponding peak positions in samples A, B and C.

3.2.1 Impact of doping and irradiation. Upon Cr doping, no additional Raman peaks were observed, confirming the effective substitution of Cr^{3+} ions into the W^{6+} lattice. Moreover, doping had minimal impact on the peak profile. However, after electron beam irradiation of the Cr–WO_3 film, distinct sharp peaks emerged. The presence of sharp and well-defined Raman peaks typically indicates a high degree of crystallinity and structural order in the material. For WO_3, characteristic peaks at 716 and 805 cm^{-1} are associated with a well-ordered monoclinic structure.[40] Fig. 4(b) presents the Voigt deconvolution of these peaks, revealing that their full-width at half-maximum (FWHM) values decrease with Cr incorporation and further narrow upon irradiation. The lowest recorded FWHM values of 48 cm^{-1} and 27 cm^{-1} for the irradiated sample suggest an enhancement in crystallinity. This improvement may be attributed to irradiation-induced stress relaxation, as observed in the XRD analysis, which contributes to the increased structural order of the films.

In addition, a slight shift of 1–6 cm^{-1} in the peak positions was observed among the doped and irradiated samples. This

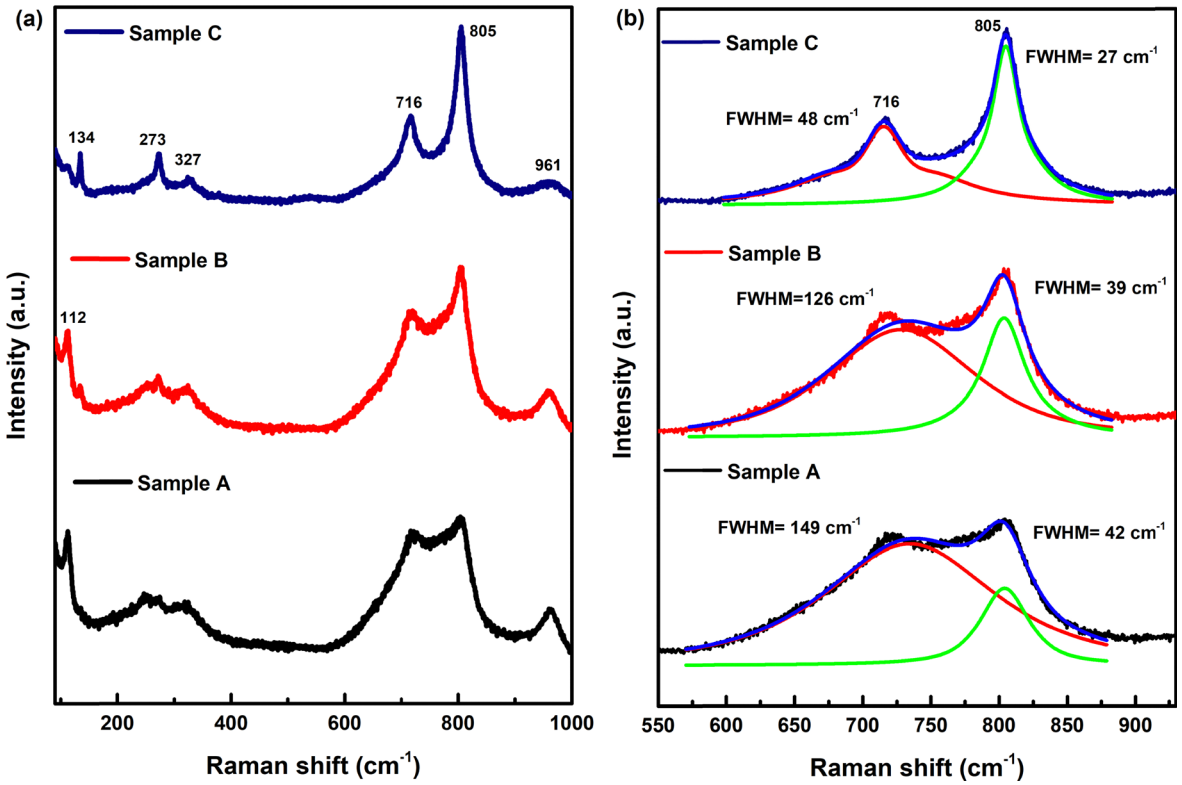

Fig. 4 (a) Raman spectra of samples A, B and C. (b) Enlarged view of deconvoluted O–W–O stretching vibrations.

Table 3 Raman peak assignments corresponding to different peak positions

	Peak position (cm^{-1})		
Peak assignments	Sample A	Sample B	Sample C
Lattice modes	111, 134	112, 134	111, 134
δ(O–W–O)	270, 321	273, 322	273, 327
ν_{as}(O–W–O), ν_s(O–W–O)	722, 803	717, 804	716, 805
ν_s(W═O)	962	959	961

shift can be attributed to multiple factors, including internal stress arising from the interaction between WO_3 atoms and the laser, atomic coupling effects, phonon confinement, and point defect-induced diffusion.[41,42] These mechanisms influence vibrational spectra, leading to subtle but measurable peak shifts. In the present case, the synergistic effect of doping and irradiation is suggested to induce point defects, such as oxygen vacancies or stress-induced distortions, which plausibly contribute to the observed peak shifts. This behaviour is consistent with previously observed trends in oxygen-deficient WO_3.[43]

3.3 Photoluminescence (PL) properties

To understand the defect contribution in the film structure, PL was conducted. Fig. 5(a)–(c) shows the deconvoluted PL spectra of the films, excited at a wavelength of 256 nm. Violet and blue emissions (2.64–3.13 eV) originate from the band–band transitions and vacant oxygen-related defects. In the present study, the bandgap determined from UV-visible spectroscopy is approximately 3.10 eV (Fig. S1(b), ESI†), which is larger than the prominent peak observed at 2.69 eV in the PL spectrum. Therefore, a major peak at 2.69 eV is assigned to electron and hole recombination from the defect energy levels such as oxygen vacancies (V_o), tungsten interstitials (W_{inter}), self-trapped excitons, and other defects in the bandgap. Upadhyay *et al.*[44] and Bhargava *et al.*[45] reported similar findings from their study. They have ascribed the blue emission to the presence of oxygen vacancies and defects located in the conduction band minimum within the fundamental bandgap. Emission at 2.64 eV is probably due to defects related to Cr^{3+} and WO_3 transitions.[46] Lower energy emissions at 2.21 eV (green) and 2.13 eV (orange) are mediated by oxygen vacancy defects (V_o^+/V_o^{++}) and deformation centers created in the crystal lattice, respectively.[47] Fig. 6(a) and (b) shows a graphical representation of the peak widths and peak positions of all the samples corresponding to different emission centers.

3.3.1 Impact of doping and irradiation. Doping or irradiation did not introduce any distinct new defect levels in the crystal lattice. However, minor variations in defect density were observed among the doped and irradiated samples. The contribution of defects can also be assessed through peak width or FWHM of the emission peaks, as defect-related emissions are often associated with broader peaks or increased FWHM values. The blue emission at 2.69 eV was observed to narrow upon doping and irradiation, suggesting a possible reduction in V_o, W_{inter}, or self-trapped excitons within the WO_3 lattice. Additionally, emissions in the yellow-orange spectral range were suppressed for samples B and

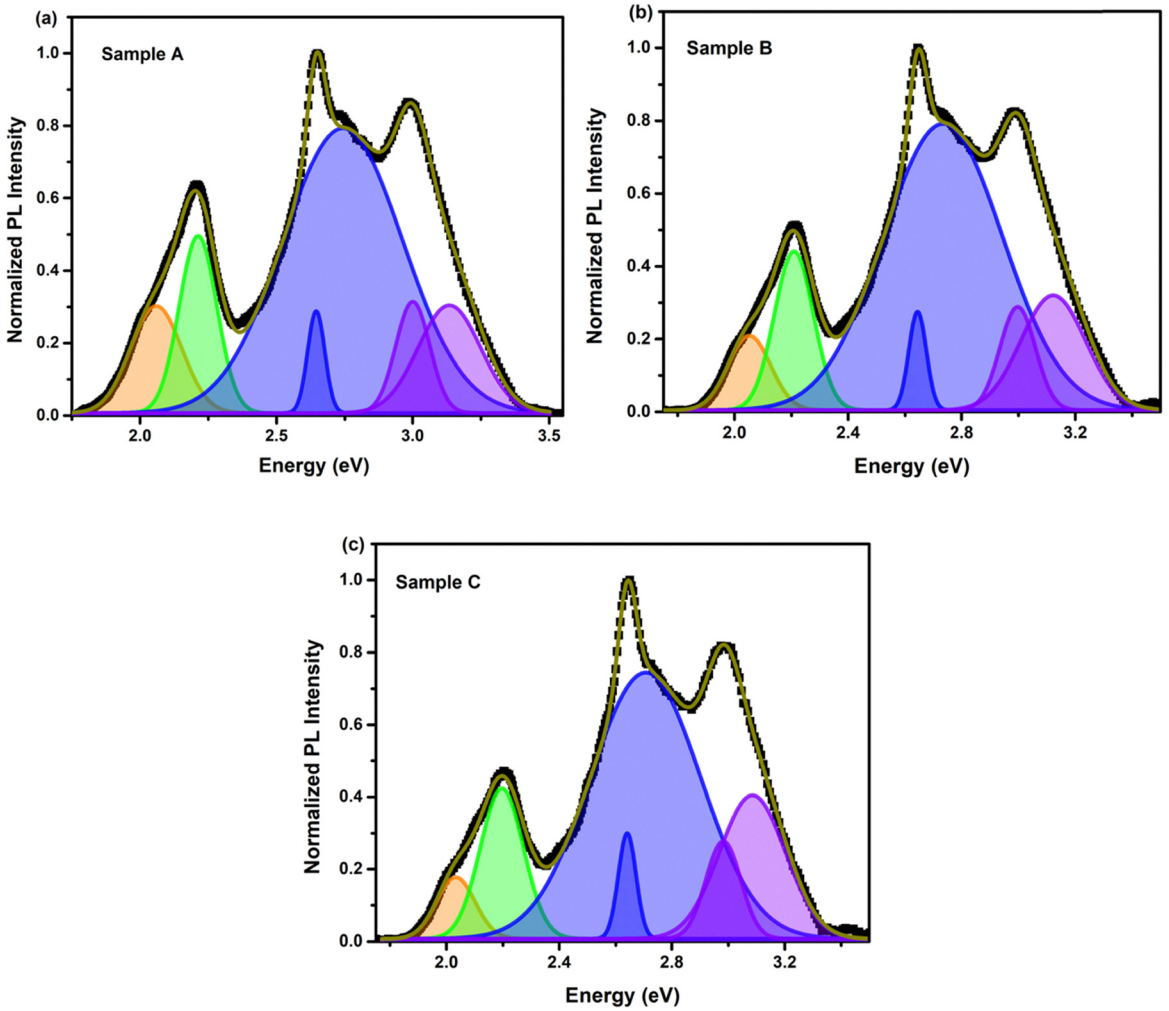

Fig. 5 (a)–(c) PL spectra of samples A, B, and C.

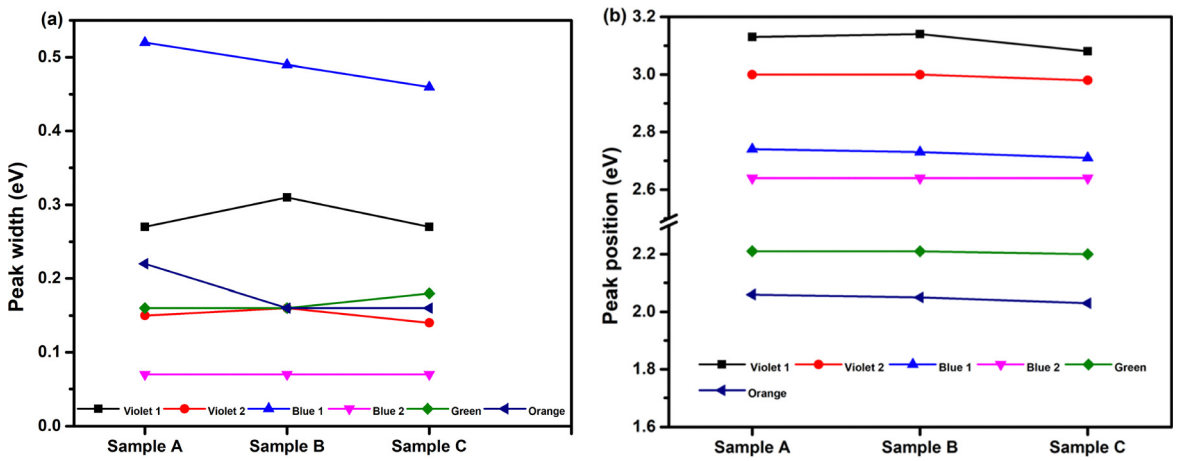

Fig. 6 Plots of (a) peak width *vs.* emission centers and (b) peak position *vs.* emission centers of samples A, B, and C.

C, which may indicate reduced lattice deformations. In contrast, a slight broadening of the green emission was noted upon irradiation. FWHM calculations for the peak at 2.21 eV suggest an increase in (V_o^+/V_o^{++}) defect concentration in the irradiated sample, with values measured at 0.16 for samples A and B and 0.18 for sample C. These results are consistent with the presence of a higher concentration of (V_o^+/V_o^{++}) defect centers in sample C compared to the others.

3.4 Morphological investigation

Fig. 7(a)–(c) present the FESEM micrographs of samples A, B and C, along with the corresponding grain distribution histogram. All films exhibited high homogeneity with no visible cracks on the surface. The undoped film possesses smaller grains, while upon doping, evenly distributed and well-defined grains became evident. Chromium induces the formation of larger nanocrystalline structures with irregular grain shapes, as illustrated in Fig. 7(b). This increase in grain size can be attributed to the role of Cr^{3+} in enhancing grain boundary mobility and reducing defect density during film growth, thereby promoting grain coalescence. A similar morphology is reported by Wang *et al.*[48] for WO_3–TiO_2 composite films. EBI led to grain fragmentation, inducing fine structures, which is visible in the morphological features shown in Fig. 7(c). The average grain sizes of the films were estimated using ImageJ software, with values determined to be 64 ± 8 nm, 72 ± 11 nm, and 51 ± 8 nm for samples A, B, and C, respectively. The irradiated sample (sample C) exhibited a smaller grain size than the others. Smaller grains provide a higher surface-to-volume ratio, facilitating faster electron exchange between grain boundaries.[9] This enhanced exchange increases the material's reactivity and gas sensitivity, as more adsorption sites are available for gas interaction.

3.5 Compositional analysis

The X-ray photoelectron spectroscopy (XPS) technique was utilized to analyze the elemental composition and oxidation states of the samples. Fig. 8(a)–(c) display the core level spectra of W 4f, while Fig. 8(d)–(f) show the O 1s core level spectra. Additionally, Fig. 8(g) and (h) illustrate the Cr 2p core level spectra for samples B and C. These spectra were calibrated using the reference C 1s peak at 284.8 eV.

3.5.1 Tungsten core level spectra. In Fig. 8(a)–(c), the W 4f core level spectra are displayed as a doublet, with two distinct components: $4f_{7/2}$ and $4f_{5/2}$ with the tungsten oxidation state of +6. These components were located at binding energies of 36.16 eV and 38.30 eV, respectively for sample A. For sample B, the peak positions were noted at 35.88 eV and 38.03 eV, while sample C exhibited peaks at 35.94 eV and 38.08 eV.[49,50] Upon doping and e-beam treatment, a slight shift in the peaks was evident, indicating the formation of sub-stoichiometric WO_3.[31] Furthermore, the satellite peak at 42.35 eV is associated with the W $5p_{3/2}$ component.

3.5.2 Oxygen core level spectra. The O 1s spectra were analyzed, revealing distinct peaks corresponding to different oxygen species (Fig. 8(d)–(f)). The primary peak (O_I), observed for all three samples at around 530.65 eV, is attributed to O^{2-} ions bonded to W^{6+} ions. The secondary peak (O_{II}) was noticed at approximately 531.43 eV, which corresponds to O^- ions or oxygen vacancies present within the lattice structure. Similarly, a third peak (O_{III}) at 532.52 eV, likely originates from chemisorbed species such as O_2^-.[51] Table 4 summarizes the peak positions and percentage area ratios of O_I, O_{II}, and O_{III}. A peak shift is observed in samples B and C, which is consistent with the W 4f core level spectra.

From a sensing perspective, oxygen vacancies serve as trap centres for incoming gas molecules and are a potential factor in enhancing gas sensing characteristics.[50] Similarly, chemisorbed species influence the sensing features as reported by Khader *et al.*[52] The present analysis indicates an increase in oxygen defects (O_{II} + O_{III}) resulting from the synergistic effects

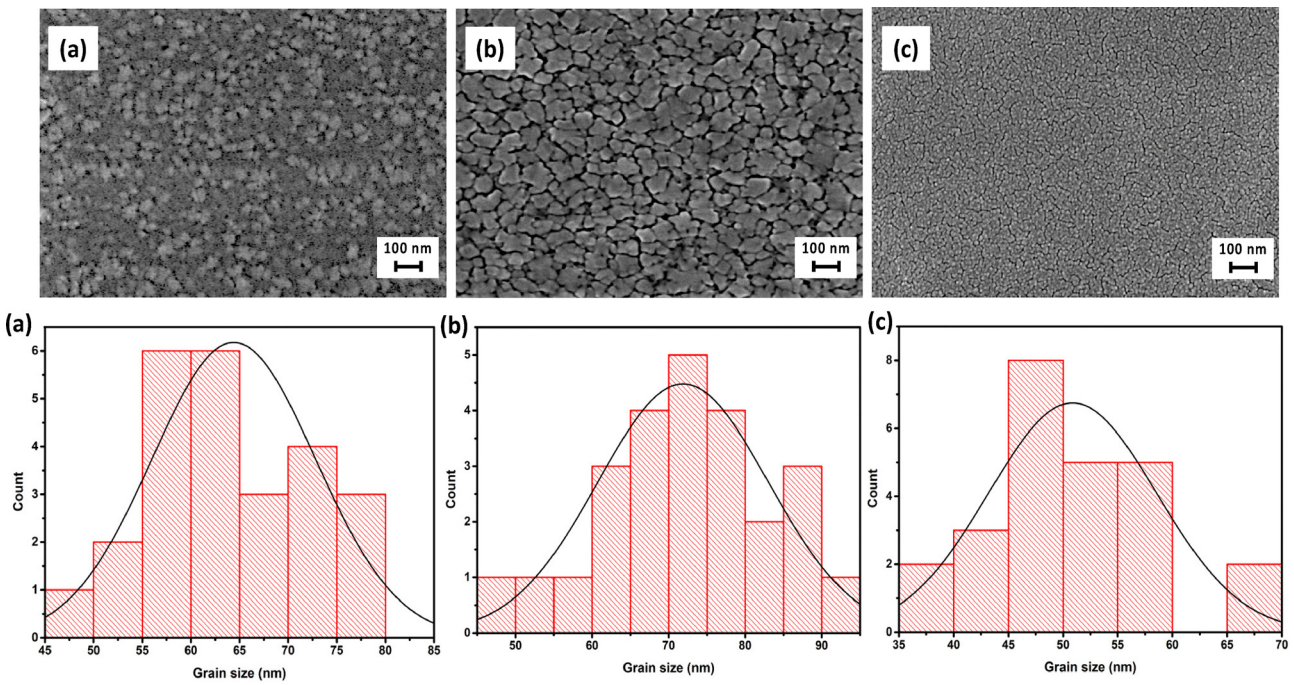

Fig. 7 (a)–(c) FESEM images and grain distribution histograms of samples A, B, and C, respectively.

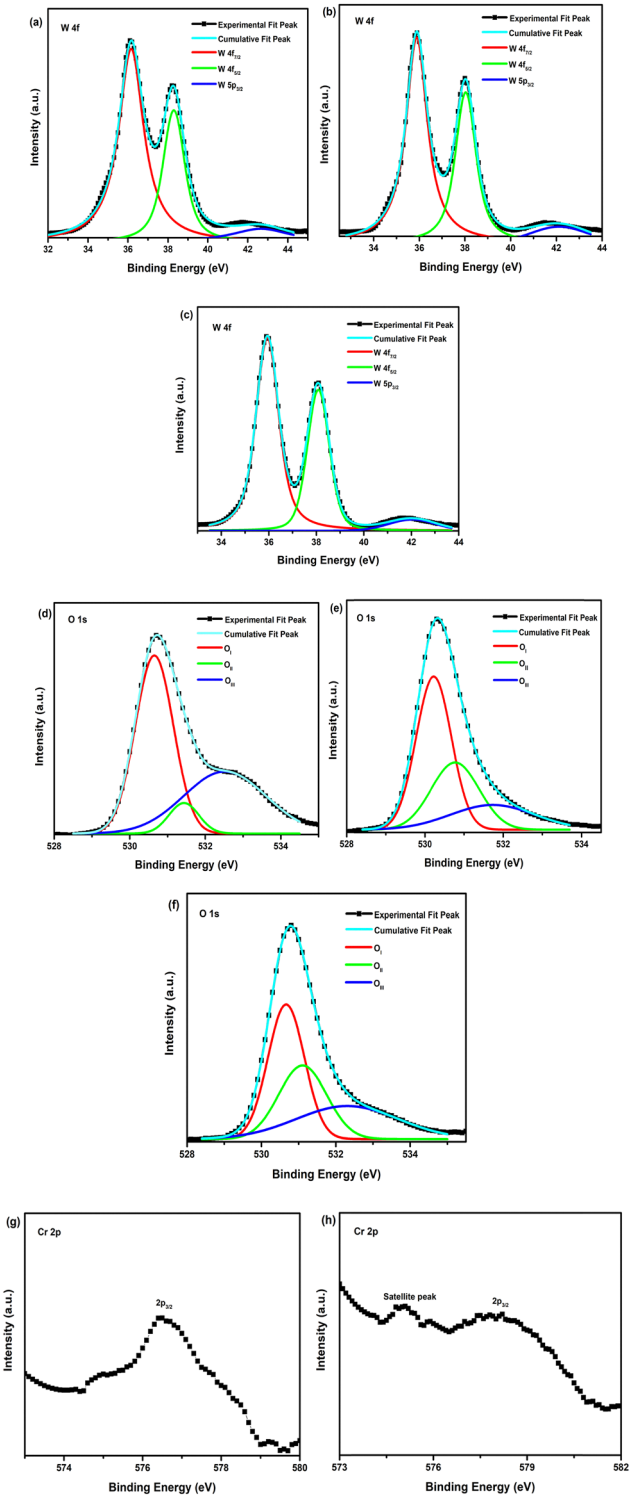

Fig. 8 Core-level spectra of (a)–(c) W 4f for samples A, B, and C, respectively; (d)–(f) O 1s for samples A, B, and C, respectively; and (g) and (h) Cr 2p for samples B and C, respectively.

of doping and irradiation. This enhancement suggests a higher concentration of oxygen-related defects in the films, particularly in sample C, which implies more favourable conditions for sensing.

Table 4 O 1s core-level spectra analysis of samples A, B, and C

Sample name	Peak	Position (eV)	Area ratio (%)
Sample A	O_I	530.65	53
	O_{II}	531.43	7
	O_{III}	532.52	40
Sample B	O_I	530.23	50
	O_{II}	530.77	28
	O_{III}	531.73	22
Sample C	O_I	530.67	41
	O_{II}	531.11	30
	O_{III}	532.31	29

3.5.3 Chromium core level spectra. The confirmation of chromium is evident from the presented spectra in Fig. 8(g) and (h), which show the Cr $2p_{3/2}$ level at a binding energy of 576.50 eV. It represents the +3 oxidation state of chromium without any other impurity phase.[53] The minor peak adjacent to the main peak in the irradiated sample is often referred to as a satellite peak and is attributable to the Cr metallic state.[54]

3.6 Gas sensing characteristics

3.6.1 NO_2 sensing measurements. Gas sensing measurements for all films were conducted in response to NO_2 at an optimized operating temperature of 200 °C. Fig. 9(a)–(c) display the transient response curves of the films at NO_2 concentrations of 1, 3, and 5 ppm. The characteristics of the curves are influenced by the type of semiconducting material and the gas to which it is exposed. Given that WO_3 displays n-type conductivity, its resistance rises upon exposure to an oxidizing gas like NO_2, and then decreases when it is returned to an air atmosphere.[55] All the films showed a noticeable response for different NO_2 concentrations. The key parameters that determine the sensor's efficiency are given in Table 5. The sensor response is a dimensionless quantity, defined as the relative ratio of resistances, and is evaluated using the equation,[23]

$$S = \left(\frac{R_g - R_a}{R_a}\right) \quad (2)$$

Here, R_a represents the resistance variation caused by the film's exposure to air, while R_g indicates the resistance change due to its exposure to NO_2.

The sensor response was boosted with the addition of chromium and further enhanced by irradiation, consistent across all NO_2 concentrations tested. As shown in Fig. 9(d), the calibration curves reveal that sample B (Cr-doped WO_3) outperforms the undoped film (sample A), and the irradiated Cr-doped film (sample C) shows the highest response. The rate of response and recovery exhibited oscillatory behaviour, with sample C achieving significantly faster kinetics. This improvement arises from a true synergy between doping and irradiation. Cr^{3+} incorporation creates additional oxygen vacancies and modifies the electronic structure to increase adsorption sites and carrier density, while subsequent electron beam irradiation refines crystallinity and optimizes defect distribution. Collectively, these

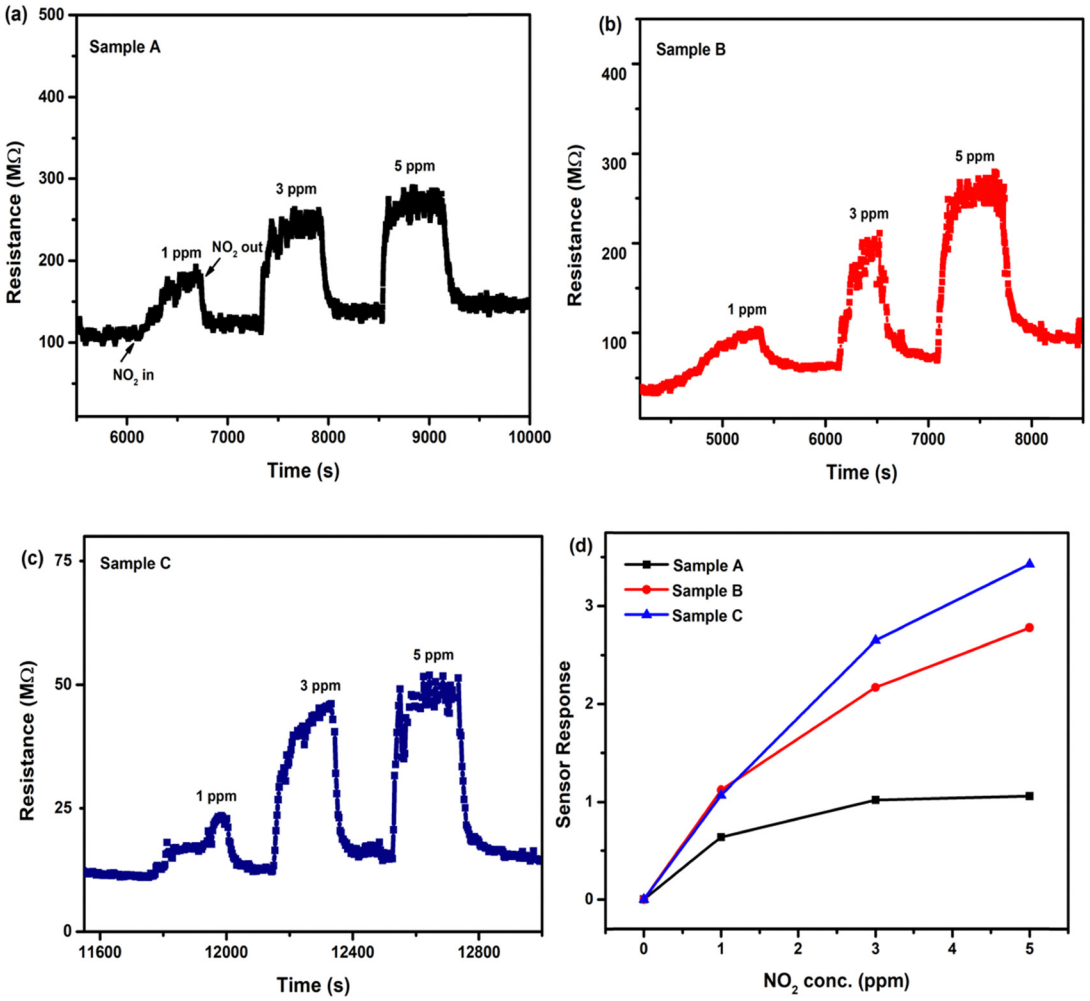

Fig. 9 (a)–(c) Transient response curves of samples A, B, and C at an operating temperature of 200 °C. (d) Corresponding calibration curves.

Table 5 Sensor parameters evaluated from the response curves

Sample name	NO_2 conc. (ppm)	Response time (s)	Recovery time (s)	Sensor response
Sample A	1	189	32	0.64
	3	85	120	1.02
	5	50	90	1.06
Sample B	1	450	188	1.12
	3	210	128	2.17
	5	75	95	2.78
Sample C	1	184	28	1.07
	3	58	23	2.65
	5	15	30	3.43

coupled effects yield a superior sensor response of 3.43 and rapid response/recovery times of 15 s/30 s at 5 ppm NO_2. This represents an overall 3.2-fold enhancement relative to the undoped film. The response and recovery characteristic curve for sample C is shown in Fig. 10(a). Theoretical limit of detection (LOD) was estimated for sample C using eqn (S4) (ESI†). It suggests that the possible lowest detection limit is 0.4 ppm (400 ppb) demonstrating the capability of sensing ultra-ppm concentration of NO_2 gas. The linear regression plot used to calculate LOD is shown in Fig. 10(b).

The enhancement in the sensor response, as well as response and recovery features, can be attributed to the following three factors:

(i) High crystallinity of the samples as evidenced by XRD and Raman analyses. Peak width analysis indicated enhanced crystallinity due to the combined effects of doping and irradiation, with sample C exhibiting higher crystalline nature. Improved crystallinity enhances the sensing performance of oxide thin films by promoting better structural order and reducing defects, thereby facilitating efficient charge transport and gas–solid interactions. This observation is consistent with previous reports emphasizing the positive influence of crystallinity on the sensitivity of metal oxide sensors.[56,57] (ii) The presence of point defects such as oxygen vacancies was confirmed through PL and XPS studies. PL spectroscopy revealed green emission bands associated with these vacancies, indicating a higher concentration of charged oxygen vacancies in sample C. Furthermore, XPS analysis supported this observation by confirming the presence of oxygen

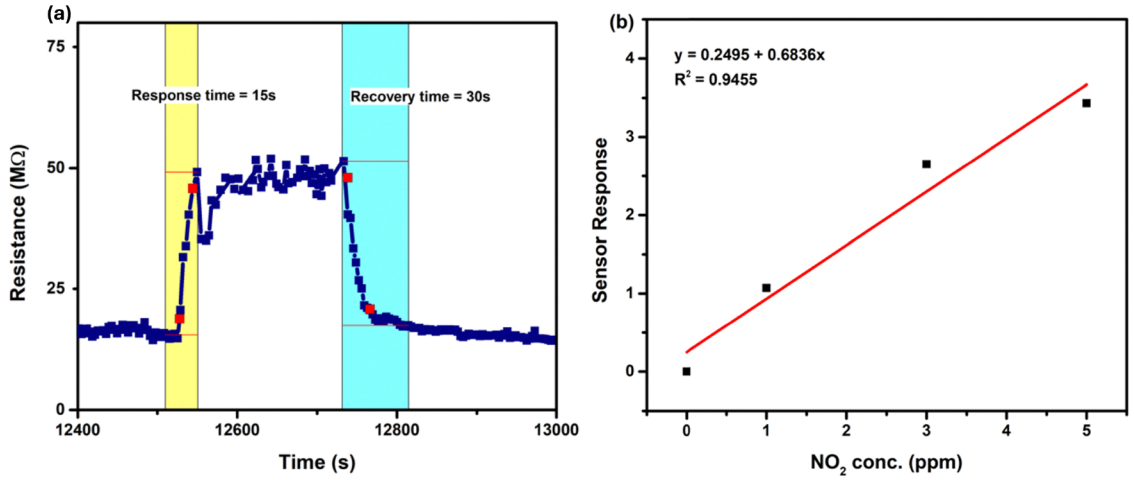

Fig. 10 (a) Response and recovery kinetics of sample C at 5 ppm NO_2 and 200 °C. (b) Linear regression graph illustrating the sensor response as a function of NO_2 concentration for sample C at 200 °C.

vacancies and chemisorbed oxygen species in the samples. Notably, the concentration of oxygen vacancies rose significantly from 7% in sample A to 28% in sample B and reached 30% in sample C. These oxygen vacancies and related species enhanced surface reactivity and provided additional active sites for gas adsorption. (iii) The smaller grain sizes of the samples ranging from 51 nm to 72 nm as seen in morphology studies. FESEM analysis showed that sample C had the smallest grains, with an average size of 51 nm. According to the *D*-2*L* model (where *D* represents grain size and *L* denotes the thickness of the electron charge layer formed on the sensor surface), smaller grains typically favour the higher gas sensitivity.[58] Together, these results suggest that the observed structural and defect-related features played a key role in the enhanced sensor performance of sample C.

Selectivity, repeatability, and stability are critical factors that determine sensor performance in practical applications. In this study, the sensing responses of sample C were evaluated for nitrogen dioxide (NO_2) and its common interfering gases including ammonia (NH_3), carbon monoxide (CO), and methane (CH_4), which are typically associated with the combustion processes. The recorded sensor responses were 3.43 for NO_2, 1.9 for NH_3, 0.21 for CO, at 5 ppm concentration and 0.22 for 50 ppm CH_4 as shown in Fig. 11(a). The results indicate that NH_3 is the most significant interferent, causing a signal attenuation of ~45%, while CO and CH_4 are the least significant interferents, resulting in a signal attenuation of ~94% at respective gas concentrations. In conclusion, sample C exhibited strong resistance to interference from NH_3, CO, and CH_4. Furthermore, repeatability test was conducted after one week, involving three cycles of NO_2 purging at a concentration of 5 ppm. Fig. 11(b) illustrates the reproducible characteristics of sample C, which exhibited consistent responses across consecutive measurements. However, it is noteworthy that the sensor response decreased by approximately 5% over the week. Thus, the present study confirms the good reproducibility and initial stability of sample C.

3.6.2 NO_2 sensing mechanism. The sensing mechanism of n-type metal oxides, such as EBI Cr–WO_3 film, upon exposure to air and NO_2 can be described as follows. When air is introduced

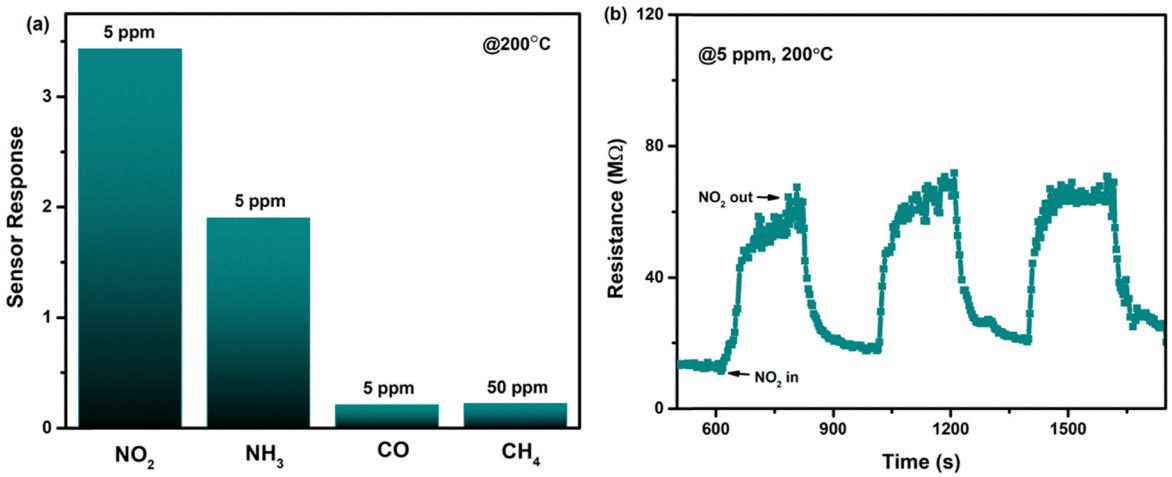

Fig. 11 (a) Selectivity histogram and (b) repeatability test performed after a week for sample C.

onto the film surface at an optimal working temperature of 200 °C, oxygen ions are drawn from the conduction band of the sensor film. Typically, O^- ions dominate within the temperature range of 150 °C to 300 °C.[59] This interaction leads to the formation of an electron charge layer (w) on the film surface and a potential barrier ($\Delta\varphi$) between the film grains, thereby reducing the film's resistance. The gas sensing mechanism and related energy band diagram are illustrated in Fig. 12, and the equations describing the oxygen adsorption phenomena are presented in eqn (3)–(5).

$$O_{2(gas)} \rightarrow O_{2(ads)} \quad (3)$$

$$O_{2(ads)} + e^- \rightarrow {O_{2(ads)}}^- \quad (4)$$

$${O_{2(ads)}}^- + e^- \rightarrow 2{O_{(ads)}}^- \quad (5)$$

When NO_2, an oxidizing gas, is introduced, it extracts electrons from the conduction band, leading to an increase in the width of the electron charge layer and the height of the potential barrier. This process results in a rise in the sensor film's resistance. The presence of a high concentration of oxygen defects (V_o ~30%), as estimated from XPS analysis, facilitates the accumulation of additional NO_2 adsorbates and enhances chemical interactions with available O^- ions, further expanding the electron charge layer and potential barrier. Consequently, the resistance increases rapidly, improving the sensor's response.[60] The equations governing NO_2 adsorption are provided in eqn (6)–(8).

$$NO_{2(gas)} \rightarrow NO_{2(ads)} \quad (6)$$

$$NO_{2(ads)} + e^- \rightarrow {NO_{2(ads)}}^- \quad (7)$$

$${NO_{2(ads)}}^- + O^- + 2e^- \rightarrow NO_{(gas)} + 2O^{2-} \quad (8)$$

Table S1 (ESI†) provides the comparison data of reported NO_2 sensors in the literature. While many WO_3-based sensors require high gas concentrations (*e.g.*, 200 ppm for mesoporous WO_3) to achieve high responses, the present study demonstrates that Cr doping and electron beam irradiation significantly enhance NO_2 sensing at a much lower concentration (5 ppm). The EB-irradiated Cr–WO_3 sensor achieves a response of 3.43, outperforming materials like Ag-doped WO_3 (1.5), WO_3 nanoflowers (2.25), and Pd–rGO (1.05). Although mesoporous WO_3 shows the highest response (99.78), it requires elevated temperatures (250–300 °C) and high NO_2 levels (200 ppm), making the present work more suitable for low-concentration detection. However, the operating temperature (200 °C) still needs further reduction, which could potentially be achieved using catalytic additives (*e.g.*, noble metals), WO_3 composites, or alternative irradiation techniques.

4. Conclusion

In this study, WO_3 films were successfully synthesized *via* spray pyrolysis, and Cr doping along with EBI was employed to enhance their NO_2 sensing performance. XRD and Raman analyses confirmed the formation of well-crystallized WO_3

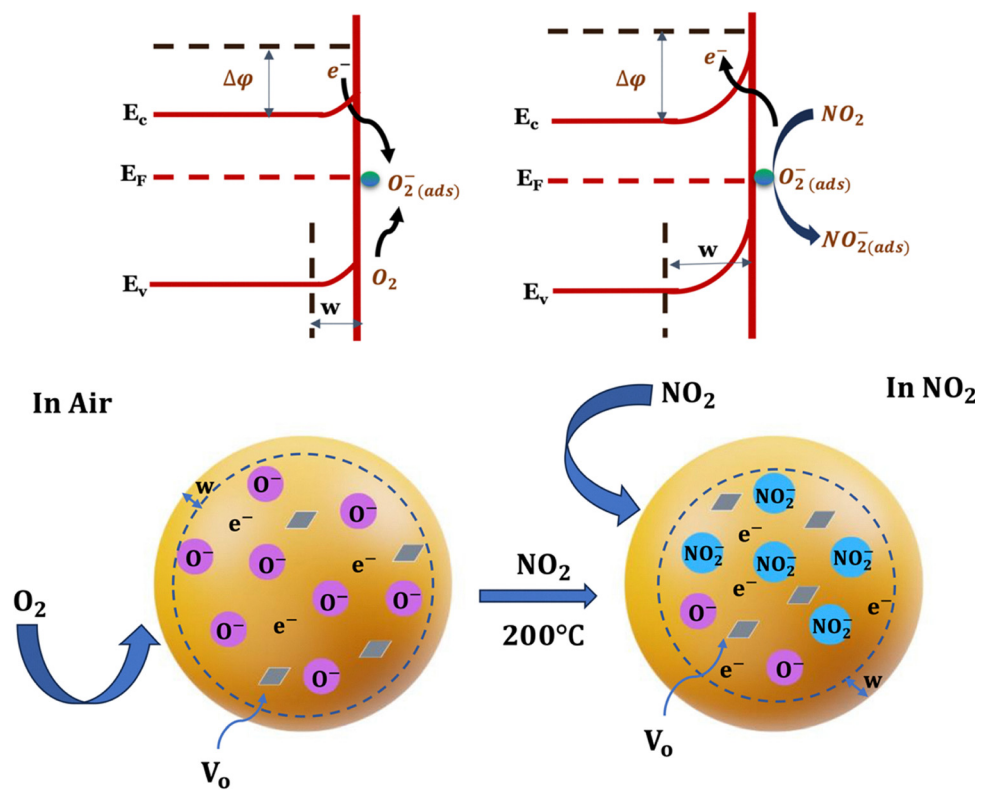

Fig. 12 Mechanism of gas sensing and band bending in EBI Cr–WO_3 film.

films. Preliminary investigations of oxygen defects using Raman and PL spectroscopy were further confirmed by XPS, which revealed a higher concentration of V_o defects in sample C. The sensor response of sample C exhibited a 3.2-fold increase compared to sample A at 5 ppm NO_2, attributed to the synergistic effects of Cr doping and EBI. Additionally, the sensor demonstrated rapid response and recovery times of 15 s and 30 s, respectively, at an optimal operating temperature of 200 °C. The enhanced sensing performance can be attributed to the presence of oxygen vacancy defects, reduced grain size, and improved crystallinity. While this work establishes a strong foundation, further studies exploring a wider range of Cr doping concentrations and EBI dosages could yield deeper insights into defect-driven sensing mechanisms, aiding in sensor optimization. Moreover, evaluating the sensor's response to a broader spectrum of target gases would help confirm its selectivity and expand its applicability across diverse gas sensing scenarios. Overall, this study presents a promising strategy for enhancing the sensing performance of WO_3-based gas sensors through the combined effects of doping and irradiation, advancing their suitability for environmental monitoring and industrial applications.

Conflicts of interest

The authors declare that they have no known competing financial interests or personal relationships that could have appeared to influence the work reported in this paper.

Data availability

The data supporting this article have been included as a part of the ESI.†

Acknowledgements

This work was supported by Manipal Academy of Higher Education, Manipal, India through Intramural Funding (Grant No.: MAHE/DREG/PhD/IMF/2019). The authors thank Prof. Sudha D. Kamath, Head, Dept. of Physics, MIT, MAHE, for providing the PL measurement facility.

References

1 Z. Li, H. Li, Z. Wu, M. Wang, J. Luo, H. Torun, P. Hu, C. Yang, M. Grundmann, X. Liu and Y. Fu, Advances in designs and mechanisms of semiconducting metal oxide nanostructures for high-precision gas sensors operated at room temperature, *Mater. Horiz.*, 2019, **6**, 470–506, DOI: **10.1039/c8mh01365a**.

2 M. Kiani, M. U. Rehman, X. Tian and B. Yakobson, Two-Dimensional Nanomaterials for the Development of Efficient Gas Sensors: Recent Advances, Challenges, and Future Perspectives, *Adv. Mater. Technol.*, 2022, **7**, 2101252, DOI: **10.1002/admt.202101252**.

3 G. M. Hingangavkar, S. A. Kadam, Y. R. Ma, S. S. Bandgar, R. N. Mulik and V. B. Patil, Tailored formation of WO_3-rGO nanohybrids for dependable low temperature NO_2 sensing, *Ceram. Int.*, 2023, **49**, 38866–38876, DOI: **10.1016/j.ceramint.2023.09.223**.

4 Ambient (outdoor) air pollution. **https://www.who.int/news-room/factsheets/detail/ambient-(outdoor)-air-quality-and-health** (accessed December 18, 2024).

5 U. Choudhari and S. Jagtap, A panoramic view of NO_x and NH_3 gas sensors, *Nano-Struct. Nano-Objects*, 2023, **35**, 100995, DOI: **10.1016/j.nanoso.2023.100995**.

6 – DTSEM – Salt Lake Technical Center O. Nitrogen Dioxide in Workplace Atmospheres. n.d.

7 C. Copat, A. Cristaldi, M. Fiore, A. Grasso, P. Zuccarello, S. S. Signorelli, G. O. Conti and M. Ferrante, The role of air pollution (PM and NO_2) in COVID-19 spread and lethality: A systematic review, *Environ. Res.*, 2020, **191**, 110129, DOI: **10.1016/j.envres.2020.110129**.

8 M. S. Choi, A. Mirzaei, H. G. Na, S. Kim, D. E. Kim, K. H. Lee, C. Jin and S. W. Choi, Facile and fast decoration of SnO_2 nanowires with Pd embedded SnO_{2-x} nanoparticles for selective NO_2 gas sensing, *Sens. Actuators, B*, 2021, **340**, 129984, DOI: **10.1016/j.snb.2021.129984**.

9 C. Wu, Y. Zhang, L. Yang, B. Xiao, A. Jiao, K. Li, T. Chen, Z. Huang and H. Lin, Flame Spray Pyrolysis Synthesis of WO_3 Sensing Materials: Effects of Flame Parameters on Particle Size Distribution and NO_2 Sensing Performance, *Langmuir*, 2022, **38**, 15506–15515, DOI: **10.1021/acs.langmuir.2c01945**.

10 S. Agarwal, P. Rai, E. N. Gatell, E. Llobet, F. Güell, M. Kumar and K. Awasthi, Gas sensing properties of ZnO nanostructures (flowers/rods)synthesized by hydrothermal method, *Sens. Actuators, B*, 2019, **292**, 24–31, DOI: **10.1016/j.snb.2019.04.083**.

11 A. M. Ruiz, G. Sakai, A. Cornet, K. Shimanoe, J. R. Morante and N. Yamazoe, Cr-doped TiO_2 gas sensor for exhaust NO_2 monitoring, *Sens. Actuators, B*, 2003, **93**, 509–518, DOI: **10.1016/S0925-4005(03)00183-7**.

12 K. M. Kim, H. M. Jeong, H. R. Kim, K. I. Choi, H. J. Kim and J. H. Lee, Selective Detection of NO_2 Using Cr-Doped CuO Nanorods, *Sensors*, 2012, **12**, 8013–8025, DOI: **10.3390/s120608013**.

13 R. Thayil and S. R. Parne, Nanostructured zinc oxide and selenide-based materials for gas sensing application: review, *J. Mater. Sci.: Mater. Electron.*, 2025, **36**, 322, DOI: **10.1007/s10854-025-14401-1**.

14 J. Yang, F. Li, Y. Zhu, Y. Yang, T. Wang, J. Huang and Y. Gui, Theoretical and experimental study on gas sensing properties of SnO_2-graphene sensor for SF_6 decomposition products, *Surf. Sci.*, 2024, **747**, 122510, DOI: **10.1016/j.susc.2024.122510**.

15 C. Dong, R. Zhao, L. Yao, Y. Ran, X. Zhang and Y. Wang, A review on WO_3 based gas sensors: Morphology control and enhanced sensing properties, *J. Alloys Compd.*, 2020, **820**, 153194, DOI: **10.1016/j.jallcom.2019.153194**.

16 H. Y. Jiang, G. L. Chen, Y. Y. Xin, S. K. Shen, Z. P. Deng, Y. M. Xu, L. H. Huo and S. Gao, Low-temperature and high-response nitric oxide sensor based on mesoporous WO_3 microtubules inherited from absorbent cottons, *Sens. Actuators, B*, 2024, **418**, 136320, DOI: **10.1016/j.snb.2024.136320**.

17 P. Ghosh, M. Manikandan, S. Sen and P. S. Devi, Some interesting insights into the acetone sensing characteristics of monoclinic WO_3, *Mater. Adv.*, 2023, **4**, 1146–1160, DOI: 10.1039/d2ma00651k.

18 D. Kanchan Kumar, P. Bharathi, J. Archana, M. Navaneethan and S. Harish, Optimizing NO_2 gas sensor performance: Investigating the influence of cobalt doping on WO_3 recovery kinetics for enhanced gas sensing application, *Sens. Actuators, B*, 2024, **421**, 136477, DOI: 10.1016/j.snb.2024.136477.

19 S. Wei, G. Chang, Y. Liu, Y. Wu, Y. Zhang, Y. Hu and W. Zhang, Heterojunction and exposed facet engineering of ZnO/WO_3 flower structure for fast and sensitive low-concentration NO_2 sensing, *Mater. Res. Bull.*, 2023, **163**, 112218, DOI: 10.1016/j.materresbull.2023.112218.

20 Y. Han, Y. Liu, C. Su, X. Chen, B. Li, W. Jiang, M. Zeng, N. Hu, Y. Su, Z. Zhou, Z. G. Zhu and Z. Yang, Hierarchical WS_2-WO_3 Nanohybrids with P-N Heterojunctions for NO_2 Detection, *ACS Appl. Nano Mater.*, 2021, **4**, 1626–1634, DOI: 10.1021/acsanm.0c03094.

21 N. Lavanya, A. C. Anithaa, C. Sekar, K. Asokan, A. Bonavita, N. Donato, S. G. Leonardi and G. Neri, Effect of gamma irradiation on structural, electrical and gas sensing properties of tungsten oxide nanoparticles, *J. Alloys Compd.*, 2017, **693**, 366–372, DOI: 10.1016/j.jallcom.2016.09.137.

22 C. Zhang, O. Van Overschelde, A. Boudiba, R. Snyders, M. G. Olivier and M. Debliquy, Improvement of sensing characteristics of radio-frequency sputtered tungsten oxide films through surface modification by laser irradiation, *Mater. Chem. Phys.*, 2012, **133**, 588–591, DOI: 10.1016/j.matchemphys.2012.01.116.

23 E. Rossinyol, A. Prim, E. Pellicer, J. Arbiol, F. Hernández-Ramírez, F. Peiró, A. Cornet, J. R. Morante, L. A. Solovyov, B. Tian, T. Bo and D. Zhao, Synthesis and characterization of chromium-doped mesoporous tungsten oxide for gas-sensing applications, *Adv. Funct. Mater.*, 2007, **17**, 1801–1806, DOI: 10.1002/adfm.200600722.

24 G. Mathankumar, P. Bharathi, M. Krishna Mohan, J. Archana, S. Harish and M. Navaneethan, Defect manipulation of WO_3 nanostructures by yttrium for ultra-sensitive and highly selective NO_2 detection, *Sens. Actuators, B*, 2022, **353**, 131057, DOI: 10.1016/j.snb.2021.131057.

25 J. S. Lee, O. S. Kwon, D. H. Shin and J. Jang, WO_3 nanomodule-decorated hybrid carbon nanofibers for NO_2 gas sensor application, *J. Mater. Chem. A*, 2013, **1**, 9099–9106, DOI: 10.1039/c3ta11658a.

26 R. Ponnusamy, A. Gangan, B. Chakraborty and C. Sekhar Rout, Tuning the pure monoclinic phase of WO_3 and WO_3-Ag nanostructures for non-enzymatic glucose sensing application with theoretical insight from electronic structure simulations, *J. Appl. Phys.*, 2018, **123**, 024701, DOI: 10.1063/1.5010826.

27 N. Zhang, C. Chen, Z. Mei, X. Liu, X. Qu, Y. Li, S. Li, W. Qi, Y. Zhang, J. Ye, V. A. L. Roy and R. Ma, Monoclinic Tungsten Oxide with {100} Facet Orientation and Tuned Electronic Band Structure for Enhanced Photocatalytic Oxidations, *ACS Appl. Mater. Interfaces*, 2016, **8**, 10367–10374, DOI: 10.1021/acsami.6b02275.

28 S. M. Altanany, M. A. Gondal and U. Baig, Synthesis and characterization of CuO/WO3 nanocomposite using hybrid method: Simple precipitation and pulsed laser ablation in liquids technique. *AIP Conf Proc*, American Institute of Physics Inc., 2018, vol. 1976, DOI: 10.1063/1.5042381.

29 S. B. Upadhyay, R. K. Mishra and P. P. Sahay, Cr-doped WO_3 nanosheets: Structural, optical and formaldehyde sensing properties, *Ceram. Int.*, 2016, **42**, 15301–15310, DOI: 10.1016/j.ceramint.2016.06.170.

30 Z. Zhu, L. Zheng, S. Zheng, J. Chen, M. Liang, Y. Tian and D. Yang, Cr doped WO_3 nanofibers enriched with surface oxygen vacancies for highly sensitive detection of the 3-hydroxy-2-butanone biomarker, *J. Mater. Chem. A*, 2018, **6**, 21419–21427, DOI: 10.1039/c8ta08670b.

31 S. M. Majhi, A. Mirzaei, S. Navale, H. W. Kim and S. S. Kim, Boosting the sensing properties of resistive-based gas sensors by irradiation techniques: A review, *Nanoscale*, 2021, **13**, 4728–4757, DOI: 10.1039/d0nr08448d.

32 K. Hlushko, A. Mackova, J. Zalesak, M. Burghammer, A. Davydok, C. Krywka, R. Daniel, J. Keckes and J. Todt, Ion irradiation-induced localized stress relaxation in W thin film revealed by cross-sectional X-ray nanodiffraction, *Thin Solid Films*, 2021, **722**, 138571, DOI: 10.1016/j.tsf.2021.138571.

33 L. Pranevicius, K. F. Badawi, N. Durand, J. Delafond and P. Goudeau, Relaxation of residual stresses in highly stressed multilayers initiated by ion irradiation, *Surf. Coat. Technol.*, 1995, **71**, 254–258, DOI: 10.1016/0257-8972(94)02321-G.

34 H. Hassani, B. Partoens, E. Bousquet and P. Ghosez, First-principles study of lattice dynamical properties of the room-temperature $P2_1/n$ and ground-state $P2_1/c$ phases of WO_3, *Phys. Rev. B*, 2022, **105**, 014107, DOI: 10.1103/PhysRevB.105.014107.

35 M. F. Daniel, J. C. Lassegues, B. Gerand and M. Fjglarz, Infrared and Raman Study of WO_3 Tungsten Trioxides and WO_3, xH_2O Tungsten Trioxide Hydrates, *J. Solid State Chem.*, 1987, **67**, 235–247, DOI: 10.1016/0022-4596(87)90359-8.

36 R. F. Garcia-Sanchez, T. Ahmido, D. Casimir, S. Baliga and P. Misra, Thermal effects associated with the Raman spectroscopy of WO_3 gas-sensor materials, *J. Phys. Chem. A*, 2013, **117**, 13825–13831, DOI: 10.1021/jp408303p.

37 K. Thummavichai, N. Wang, F. Xu, G. Rance, Y. Xia and Y. Zhu, In situ investigations of the phase change behaviour of tungsten oxide nanostructures, *R. Soc. Open Sci.*, 2018, **5**, 171932, DOI: 10.1098/rsos.171932.

38 R. Mukherjee, C. S. Prajapati and P. P. Sahay, Tailoring the microstructural, optical, and electrical properties of nanocrystalline WO_3 thin films using Al doping, *J. Mater. Eng. Perform.*, 2014, **23**, 3141–3151, DOI: 10.1007/s11665-014-1094-5.

39 Y. Shigesato, A. Murayama, T. Kamimori and K. Matsuhiro, Characterization of evaporated amorphous WO_3 films by Raman and FTIR spectroscopies, *Appl. Surf. Sci.*, 1988, **33**, 804–811, DOI: 10.1016/0169-4332(88)90384-4.

40 V. B. Kumar and D. Mohanta, Formation of nanoscale tungsten oxide structures and colouration characteristics, *Bull. Mater. Sci.*, 2011, **34**, 435–442, DOI: 10.1007/s12034-011-0117-1.

41 A. K. Arora, M. Rajalakshmi, T. R. Ravindran and V. Sivasubramanian, Raman spectroscopy of optical phonon confinement in nanostructured materials, *J. Raman Spectrosc.*, 2007, **38**, 604–617, DOI: 10.1002/jrs.1684.
42 S. Agarwal, Q. Chen, T. Koyanagi, Y. Zhao, S. J. Zinkle and W. J. Weber, Revealing irradiation damage along with the entire damage range in ion-irradiated SiC/SiC composites using Raman spectroscopy, *J. Nucl. Mater.*, 2019, **526**, 151778, DOI: 10.1016/j.jnucmat.2019.151778.
43 P. J. Boruah, R. R. Khanikar and H. Bailung, Synthesis and Characterization of Oxygen Vacancy Induced Narrow Bandgap Tungsten Oxide (WO_{3-x}) Nanoparticles by Plasma Discharge in Liquid and Its Photocatalytic Activity, *Plasma Chem. Plasma Process.*, 2020, **40**, 1019–1036, DOI: 10.1007/s11090-020-10073-3.
44 S. B. Upadhyay, R. K. Mishra and P. P. Sahay, Cr-doped WO_3 nanosheets: Structural, optical and formaldehyde sensing properties, *Ceram. Int.*, 2016, **42**, 15301–15310, DOI: 10.1016/j.ceramint.2016.06.170.
45 R. Bhargava and S. Khan, Fabrication of WO_3–reduced graphene oxide (WO_3–G) nanocomposite for enhanced optical and electrical properties, *J. Mater. Sci.: Mater. Electron.*, 2020, **31**, 8370–8384, DOI: 10.1007/s10854-020-03372-0.
46 A. Jerold Antony, S. Mary Jelastin Kala, C. Joel, R. Biju Bennie and S. Vivetha, Structural, optical, and magnetic properties of pristine and Cr doped WO_3 nanoparticles, *Inorg. Nano-Met. Chem.*, 2022, **52**, 951–960, DOI: 10.1080/24701556.2021.2025395.
47 A. Yadav, A. Sharma, V. Baloria, P. Singh and G. Gupta, Ultrahigh sensitive NO sensor based on WO_3 film with ppb-level sensitivity, *Ceram. Int.*, 2023, **49**, 7853–7860, DOI: 10.1016/j.ceramint.2022.10.284.
48 L. Wang, L. Yuan, X. Wu, J. Wu, C. Hou and S. Feng, Electrochromic response of pulsed laser deposition prepared WO_3-TiO_2 composite film, *RSC Adv.*, 2014, **4**, 47670–47676, DOI: 10.1039/c4ra07138g.
49 L. Wang, A. U. Rehman, H. Wu, B. Wu, L. Li and K. Shi, Submicrochains composed of massage ball-like WO_3@$CuWO_4$ composites for high-efficiency CO gas sensing applications at room temperature, *RSC Adv.*, 2016, **6**, 69999–70007.
50 W. Yu, Z. Shen, F. Peng, Y. Lu, M. Ge, X. Fu, Y. Sun, X. Chen and N. Dai, Improving gas sensing performance by oxygen vacancies in sub-stoichiometric WO_{3-x}, *RSC Adv.*, 2019, **9**, 7723–7728, DOI: 10.1039/c9ra00116f.
51 A. P. Shpak, A. M. Korduban, M. M. Medvedskij and V. O. Kandyba, XPS studies of active elements surface of gas sensors based on WO_{3-x} nanoparticles, *J. Electron Spectrosc. Relat. Phenom.*, 2007, **156**, 172–175, DOI: 10.1016/j.elspec.2006.12.059.
52 M. M. Khader, M. M. Saleh and A. M. Mohammad, Studies of the Adsorption of SO_2 H_2 and O_2, on a Cr_2O_3 Surface by an Electrical Conductivity Technique, *Adsorpt. Sci. Technol.*, 1999, **17**, 375–387, DOI: 10.1177/026361749901700503.
53 Y. Wang, B. Liu, S. Xiao, X. Wang, L. Sun, H. Li, W. Xie, Q. Li, Q. Zhang and T. Wang, Low-Temperature H_2S Detection with Hierarchical Cr-Doped WO_3 Microspheres, *ACS Appl. Mater. Interfaces*, 2016, **8**, 9674–9683, DOI: 10.1021/acsami.5b12857.
54 M. C. Biesinger, B. P. Payne, A. P. Grosvenor, L. W. M. Lau, A. R. Gerson and R. S. C. Smart, Resolving surface chemical states in XPS analysis of first row transition metals, oxides and hydroxides: Cr, Mn, Fe, Co and Ni, *Appl. Surf. Sci.*, 2011, **257**, 2717–2730, DOI: 10.1016/j.apsusc.2010.10.051.
55 H. Zhang, Y. Wang, X. Zhu, Y. Li and W. Cai, Bilayer Au nanoparticle-decorated WO_3 porous thin films: On-chip fabrication and enhanced NO_2 gas sensing performances with high selectivity, *Sens. Actuators, B*, 2019, **280**, 192–200, DOI: 10.1016/j.snb.2018.10.065.
56 G. Korotcenkov, The role of morphology and crystallographic structure of metal oxides in response of conductometric-type gas sensors, *Mater. Sci. Eng., R*, 2008, **61**, 1–39, DOI: 10.1016/j.mser.2008.02.001.
57 E. Comini, Metal oxides nanowires chemical/gas sensors: recent advances, *Mater. Today Adv.*, 2020, **7**, 100099, DOI: 10.1016/j.mtadv.2020.100099.
58 A. Rothschild and Y. Komem, The effect of grain size on the sensitivity of nanocrystalline metal-oxide gas sensors, *J. Appl. Phys.*, 2004, **95**, 6374–6380, DOI: 10.1063/1.1728314.
59 J. He, H. Meng, Y. Xu and L. Feng, Hollow mesoporous In_2O_3 derived from MIL-68 (In) for dual gas sensing of NO_2 and H_2, *Sens. Actuators, B*, 2024, **418**, 136336, DOI: 10.1016/j.snb.2024.136336.
60 H. Lin, J. Wang, S. Xu, Q. Zhang, Y. Cheng, D. Han, H. Wang and K. Zhuo, Au-WO_3 Nanowire-Based Electrodes for NO_2 Sensing, *ACS Appl. Nano Mater.*, 2022, **5**, 14311–14319, DOI: 10.1021/acsanm.2c02289.